NASA Technical Memorandum 83658

NASA-TM-83658

19840016951

Optimization of Fringe-Type Laser Anemometers for Turbine Engine Component Testing
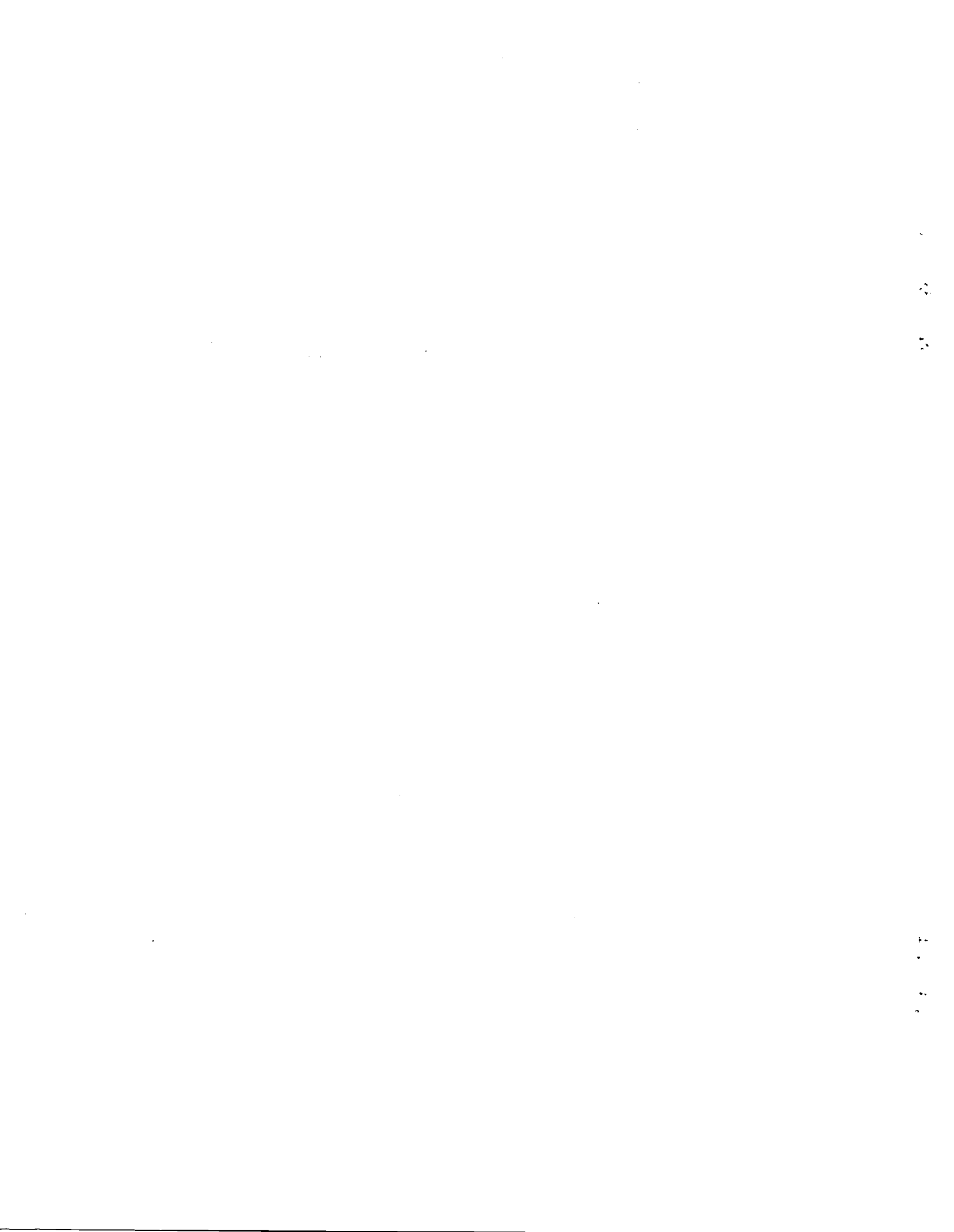
Richard G. Seasholtz, Lawrence G. Oberle,
and Donald H. Weikle
Lewis Research Center
Cleveland, Ohio

NASA

AIAA'84

Richard G. Seasholtz, Lawrence G. Oberle
and Donald H. Weikle, Lewis Research Center
Cleveland, OH

N84-25019#

OPTIMIZATION OF FRINGE-TYPE LASER ANEMOMETERS FOR TURBINE ENGINE COMPONENT TESTING

Richard G. Seasholtz, Lawrence G. Oberle, and Donald H. Weikle
National Aeronautics and Space Administration
Lewis Research Center
Cleveland, Ohio 44135

Abstract

The fringe-type laser anemometer is analyzed using the Cramer-Rao bound for the variance of the estimate of the Doppler frequency as a figure-of-merit. Mie scattering theory is used to calculate the Doppler signal wherein both the amplitude and phase of the scattered light are taken into account. The noise from wall scatter is calculated using the wall bidirectional reflectivity and the irradiance of the incident beams. A procedure is described to determine the optimum aperture mask for the probe volume located a given distance from a wall. The expected performance of counter-type processors is also discussed in relation to the Cramer-Rao bound. Numerical examples are presented for a coaxial backscatter anemometer.

Nomenclature

a	expected peak pedestal counts per Doppler cycle
A	expected peak pedestal counts per second
c	velocity of light
$<>$	expected value of
$\underline{E}$	electric field vectors
E_0	electric field amplitude
f_β	frequency difference between incident beams, Hz
f_D	Doppler frequency, Hz
F	lens focal length
h	Planck's constant
$I(x,y)$	irradiance at point (x,y)
k	wave number ($= |\underline{k}|$)
$\underline{k}_{1,2}$	wave vectors of incident beams
$\underline{k}_s$	wave vector of scattered light
L_r	radiance of laser light reflected by wall
L_b	radiance of background light
$\underline{n}$	measurement set vector
n_i	number counts in ith time interval
n_0	expected noise, counts per Doppler cycle
$n(x,y)$	noise defined by eq. (10)
n_k	noise counts due to flux through k th area element (eq. (21))
N_f	number fringes between $1/e^2$ irradiance points
N_0	expected value of noise from wall scatter and background
$\hat{p}_{1,2}$	unit vectors normal to incident beams and in scattering planes
$p(x,y)$	pedestal signal defined by eq. (11)
$p(\underline{\alpha}|\underline{n})$	likelihood function
p_0	integral of $p(x,y)$ over aperture
P_ℓ	laser power
$\hat{q}_{1,2}$	unit vectors normal to scattered beam and in scattering planes
$q(x,y)$	signal defined by eq. (11)
q_0	integral of $q(x,y)$ over aperture
q_k	signal counts due to flux through k th area element (eq. (21))
Q	quality factor defined by eq. (22)
R	distance from scatterer to observation point
$\hat{s}_{1,2}$	unit vectors normal to scattering planes
$s(x,y)$	signal defined by eq. (11)
s_0	integral of $s(x,y)$ over aperture
s_k	signal counts due to flux through k th area element (eq. (21))
$S_\alpha(\theta)$	Mie scattering amplitude function (α = "s", "p")
SNR	signal-to-noise ratio
t	time, sec
t_0	time at peak of Doppler burst, sec
V	visibility of Doppler burst
$\mathcal{V}(\ )$	variance of $(\ )$
w	beam radius at $1/e^2$ irradiance point
w_0	beam waist radius
Z_0	intrinsic impedance of free space
α_i	ith unknown parameter
β	half of beam crossing angle
$\underline{\underline{\Gamma}}$	Fisher information matrix
$\delta_\alpha(\theta)$	phase of scattering light (α = "s", "p")
$\delta_{\alpha\beta}$	phase difference of light scattered from two beams (eq. (B13))
ΔA	area element in aperture plane
Δf	system noise bandwidth
Δt	time interval
η	quantum efficiency
θ	angular coordinate

$\theta_{1,2}$	scattering angles
λ	wavelength of laser light
ρ'	bidirectional reflectivity
$\sigma_{\alpha\beta}$	scattering cross sections defined by eq. (B13)
σ_{fD}	standard deviation of estimate of Doppler frequency
ϕ	angular coordinate
ϕ_f	flow angle relative to fringe normals
ψ	phase of Doppler signal
Ω'	solid angle subtended by pinhole image at point in aperture planel

Introduction

The laser anemometer (LA) has become a valuable tool in turbine engine research, providing data that would be almost impossible to gather using conventional instrumentation. However, this application of LA has proven to be one of its more difficult. Measurements in turbomachinery components are typified by small passages and highly accelerated, high velocity flows. This leads to the requirement for small seed particles that will faithfully follow the flow. Unfortunately, small particles are weak light scatterers, which result in low signal levels. When coupled with the high level of noise caused by laser light scattered from surfaces near the measurement point, the signal-to-noise ratio (SNR) is often less than needed for accurate determination of the particle velocity.

Limitations of the conventional dual-beam fringe-type LA have forced researchers to look for new techniques and new optical designs.

In particular, the dual-focus (two-spot) LA was developed[1] for use in engine research. This system is more sensitive to small particles and has better stray light rejection properties than the fringe LA. However, the dual-focus LA generally is more expensive and requires more sophisticated signal processing than the fringe LA. Also, in highly turbulent flows, the data rate tends to be lower than the data rate achieved with the fringe LA. (This low data problem may be solved by use of elliptical spot systems such as described in ref. 2.)

One technique that has permitted the fringe LA to be successfully used in compressor and turbine testing[3-6] is the use of fluorescent seed particles.[3-6] The laser-induced fluorescence from the particles is separated from the laser light scattered from walls by an optical filter. This allows measurements to be made close to surfaces. Unfortunately, the fluorescent efficiency of the dyes used decreases rapidly as the temperature of the flow increases above room temperature. Thus, unless a high efficiency, high temperature fluorescent seed material is found, it appears that this technique will not be usable for high temperature flows.

Another approach[7,8] for making measurements close to walls with the fringe LA is based on using the differences of the polarization properties of the light scattered from particles and from solid surfaces. However, the success of this technique depends on the assumption of nonabsorbing spherical particles and on the details of the surface, such as roughness and the presence of deposits.

In spite of its limitations, we feel that the fringe LA is suitable for many turbine engine component tests. For this reason, a detailed analysis of the fringe LA was conducted with the purpose of defining its limits of applicability. This paper addresses the problem of optimizing the optical system to achieve the best measurement of the velocity of a single seed particle. Note that this is only one part of the overall problem of the rapid, accurate determination of the flow parameters in turbine engine components. Other factors must also be considered, such as statistical biasing and proper data reduction methods.

In this paper, the fringe-type laser anemometer is analyzed using the Cramer-Rao bound for the variance of the estimate of the Doppler frequency as a figure-of-merit. The noise from wall scatter is calculated using the wall bidirectional reflectivity and the irradiance of the incident beams. Mie scattering theory is used to calculate the Doppler signal.

Similar work has been reported[9,10] for evaluating the signal-to-noise ratio for measurements close to walls. That work is extended here by treating the particle scattering using Mie scattering theory (instead of assuming a constant cross section) and by characterizing the wall reflectivity by the bidirectional reflectivity (instead of assuming a constant value for the reflectivity). Thus the analysis presented here can be used to evaluate the effect of various wall treatments and coatings which have reflectivities that are a function of both the incident light direction and the observation direction.

In addition, a procedure is presented for determining the optimum aperture mask for the probe volume located a given distance from a wall. The use of circular aperture masks to decrease probe volume length has been recognized[11] and used in LA systems for compressor and turbine studies[3-6]. However, the procedure presented here determines the optimum mask, which is not necessarily circular.

Because the counter-type processor is usually used with fringe LA's for high velocity flows, the relation between the Cramer-Rao bound and the required signal-to-noise ratio for counters is discussed.

Finally, numerical examples for a coaxial backscatter LA are presented to illustrate the procedure for determining the optimum aperture mask.

Theory

In this section the Cramer-Rao lower bound for the variance of the estimate of the Doppler frequency will be obtained in terms of the parameters of the Doppler burst. The parameters related to the signal will be determined using Mie scattering theory. The noise parameter will be determined

by evaluating the laser light scattered by walls located near the probe volume. Finally, the performance of the counter-processor will be related to the Cramer-Rao bound.

Doppler Burst Signal

A particle passing through the probe volume of a dual-beam fringe-type laser anemometer (fig. 1) with the indicated trajectory (described by δ, the distance of closest approach to the probe volume axis, and by ϕ_f, the angle between the flow direction and the fringe normals) will generate a Doppler burst signal (assumed to be detected with a photomultiplier tube)

$$\langle n_k \rangle = A \, e^{-2\left[\frac{2f_D(t_k - t_0)}{N_f \cos \phi_f}\right]^2}$$

$$\left\{ 1 + V \cos \left[2\pi \, (f_D + f_B) \, (t_k - t_0) + \psi \right] \right\} \Delta t + N_0 \Delta t \tag{1}$$

where $\langle n_k \rangle$ is the expected number of photoelectron counts in the time interval $(t_k - \Delta t/2, t_k + \Delta t/2)$, t_0 is the time at the peak of the Gaussian envelope, f_D is the "Doppler" frequency, f_B is the frequency difference between the two incident beams, V is the visibility, N_0 is the constant background noise, $N_f = 2 \, w_0/s$ is the number of fringes, (w_0 is the waist radius of the incident beams and s is the fringe spacing) and

$$A = A_0 e^{-2(\delta/w_0)^2} \tag{2}$$

is the peak value of the pedestal, where A_0 is the peak value if the trajectory passes through the center of the probe volume. The trajectory is assumed to be near the focal plane and to have no significant component along the optical axis. The particle is assumed to have constant velocity as it passes through the probe volume.

Cramer-Rao Lower Bound

The unknown parameters in the Doppler burst can be denoted by the vector $\underset{\sim}{\alpha} = (f_D, \phi_f, t_0, A, \psi, N_0, V)$. The measurement can be described by the vector $\underset{\sim}{n} = (n_1, n_2, n_3, ..., n_k)$ with elements that are the photoelectron counts for k equal time intervals Δt.

The Cramer-Rao lower bound for the variance of the estimate of the parameter $\hat{\alpha}_i$ is[12]

$$\mathcal{V}(\hat{\alpha}_i) = (\underset{\sim}{\Gamma}^{-1})_{ii} \tag{3}$$

where $\underset{\sim}{\Gamma}$ is the Fisher information matrix with elements given by

$$\Gamma_{ij} = - \left\langle \frac{\partial^2 \ln p(\underset{\sim}{n}|\underset{\sim}{\alpha})}{\partial \alpha_i \, \partial \alpha_j} \right\rangle \tag{4}$$

The conditional probability function $p(\underset{\sim}{n}|\underset{\sim}{\alpha})$ is the likelihood function, which expresses the probability that given a set of parameters $\underset{\sim}{\alpha}$, the set of observations $\underset{\sim}{n}$ will occur. (The maximum likelihood estimate for the parameters $\underset{\sim}{\alpha}$ is given by

the $\underset{\sim}{\alpha}$ that maximizes $p(\underset{\sim}{n}|\underset{\sim}{\alpha})$ for a given set of measurements $\underset{\sim}{n}$.)

For Poisson statistics, the probability of n_k counts in one time interval is

$$p(n_k) = e^{-\langle n_k \rangle} \langle n_k \rangle^{n_k} / n_k! \tag{5}$$

where the expected value $\langle n_k \rangle$ is given by Eq. (1). The elements of Fisher information matrix can then be written[13]

$$\Gamma_{ij} = \sum_k \frac{1}{\langle n_k \rangle} \frac{\partial \langle n_k \rangle}{\partial \alpha_i} \frac{\partial \langle n_k \rangle}{\partial \alpha_j} \tag{6}$$

If the parameters are uncorrelated, the variance of the estimate of one of the parameters is given simply by the inverse of the corresponding diagonal element the Fisher information matrix; i.e., by the variance that would apply if only one parameter were unknown.

$$\mathcal{V}(\hat{\alpha}_i) \geq 1/\Gamma_{ii} \tag{7}$$

Here, we assume that the parameters are only weakly correlated, so that this much simpler relation for the Cramer-Rao bound may be used.

If we assume that the background noise is greater than the peak signal, and that the number of fringes is large compared to one, we can let $\Delta t \to 0$ and convert the sum in Eq. (6) to an integral, which can be evaluated to give a lower bound for the variance of the estimate of the Doppler frequency

$$\mathcal{V}(\hat{f}_D) \geq \frac{64}{\pi^{5/2}} \frac{N_0 f_D^3}{V^2 A^2 N^3} \tag{8}$$

where we let $N = N_f \cos \phi_f$; i.e, N is the number of cycles between the $1/e^2$ times of the envelope of the burst. Note that the lower bound is not dependent on the frequency shift f_B. Equation (8) can be rewritten to give a lower bound for the relative error (corresponding to the Cramer-Rao bound) of measurements of the Doppler frequency

$$\left(\frac{\sigma_{f_D}}{f_D}\right) = \frac{8}{\pi^{5/4}} \frac{n_0^{1/2}}{a V N^{3/2}} \tag{9}$$

where $\sigma_{f_D} = [\mathcal{V}(f_D)]^{1/2}$ and where $n_0 = N_0/f_D$ and $a = A/f_D$ are the expected noise and signal counts per Doppler period.

A comparison (for a particular set of parameters) between a numerical evaluation of (σ_{f_D}/f_D) using the full Fisher information matrix (eq. (6)), and the analytical expression (eq. (9)), is shown in Fig. 2. This indicates that the assumptions used in the derivation of Eq. (9) are valid for $n_0/aV > 2$. The simple expression for the error bound (eq. (9)) will be used in the remainder of this paper.

The task now is -- given a particular optical configuration, seed particle, test environment, and flow -- to calculate the signal and noise. We

3

then can use the lower bound of the relative error given by Eq. (9) as a figure-of-merit for this particular optical configuration. The optical configuration may then be optimized to find the maximum value of the lower bound (i.e., the smallest error in the measurement).

Noise

The background noise caused by laser light scattered from surfaces near the probe volume is a function of the optical configuration, the reflectance properties of the wall, and the distance of the wall from the probe volume. In addition to this direct wall scatter, there generally will also be a constant background noise flux caused by multiple reflections of the laser light, ambient light, and blackbody radiation from hot surfaces.

The light flux through area dA at a point (x,y) on the aperture plane due to wall scatter and background radiance is obtained in Appendix A by integrating the radiance L of the wall over the solid angle subtended by the image of the pinhole at the point on the aperture (fig. 3). This light flux, expressed in terms of photoelectron counts per Doppler cycle is (eq. A1)

$$n(x,y)dA =$$

$$\left(\frac{n\lambda}{hc\,f_D}\right)_{\Omega'} \left[L_r(x,y;\,\theta_r,\phi_r) + L_b\right]\,d\Omega\,\cos\theta\,dA \qquad (10)$$

For purposes of calculation, the aperture plane is assumed to be at the plane of the focusing lens instead of the position shown in Fig. 1 (the mask will have the same effect in either location). Also, for this calculation, we treat the laser light as if it were incoherent. This means that interference effects, such as speckle, are not taken into account. But the results obtained do represent the expected values.

Signal

For the geometry shown in Fig. 4, the signal is calculated in Appendix B using Mie scattering theory. The light flux through differential area element dA located in the aperture plane at position (x,y) consists of the following: the quadrature components of the Doppler modulated signal, $s(x,y)$ and $q(x,y)$; and the pedestal component, $p(x,y)$. These are expressed in terms of the number of counts/Doppler period as

$$s(x,y)dA = (2I_0/F^2)(n\lambda/hcf_D)\,\cos^3\theta \sum_{\alpha,\beta}\sigma_{\alpha\beta}\cos\delta_{\alpha\beta}dA$$

$$q(x,y)dA = (2I_0/F^2)(n\lambda/hcf_D)\,\cos^3\theta \sum_{\alpha,\beta}\sigma_{\alpha\beta}\sin\delta_{\alpha\beta}dA$$

$$p(x,y)dA = (2I_0/F^2)(n\lambda/hcf_D)\,\cos^3\theta\,I_{sdc} \qquad (11)$$

The calculation takes into account both the variation in the amplitude and in the phase of the scattered fields as a function of scattering angle. Examples of the variation of the differential scattering cross section and phase angles are shown in Fig. 5 for 0.5, 1.0, and 1.5 μm diameter polystyrene latex particles (refractive index = 1.59). The figure shows that for near backscatter the "p"

polarized scattering is stronger than the "s" polarized scattering. Also, it can be seen that the phase angle variation is much larger for the larger particle. This phase variation is important because it leads to a reduction in the visibility of the Doppler burst when the signal is integrated over the aperture.

Evaluation of Cramer-Rao Lower Bound

The relations derived above for noise and signal are now used to evaluate the relative error given by Eq. (9) for a given optical configuration, seed particle, and test environment.

By integrating over the clear aperture (not including light blocked by the aperture mask), we obtain the total number of counts for the two quadrature signals, the pedestal, and the background noise:

$$s_0 = \int s(x,y)dA$$

$$q_0 = \int q(x,y)dA$$

$$p_0 = \int p(x,y)dA \qquad (12)$$

$$n_0 = \int n(x,y)dA$$

These quantities are identified with the corresponding quantities in Eq. (1) for the Doppler burst signal; i.e.,

$$A/f_D = a = p_0 \qquad (13)$$

is the pedestal component,

$$AV/f_D = aV = \left(s_0^2 + q_0^2\right)^{1/2} \qquad (14)$$

is the component modulated at the Doppler frequency,

$$V = \left(s_0^2 + q_0^2\right)^{1/2}/p_0 \qquad (15)$$

is the visibility, and

$$\psi = \tan^{-1}\left(q_0/s_0\right) \qquad (16)$$

is the phase.

For the background noise dominated case (for which Eq. (9) is valid), the Cramer-Rao lower bound for uncertainty in the measurement of the Doppler frequency is thus

$$\left(\frac{\sigma_{f_D}}{f_D}\right) = \frac{8}{\pi^{5/4}\,N^{3/2}}\left(\frac{n_0}{s_0^2 + q_0^2}\right)^{1/2} \qquad (17)$$

Counter-processor

The above analysis gives a lower bound for the uncertainty in the measurement of the velocity of a single particle (eq. (17)). In practice, this error bound cannot actually be achieved. In particular, the counter-processor exhibits a threshold at a signal-to-noise ratio (SNR) of about 10.[14] For SNR > 10 the counter can be expected to give

4

good results, but below this level the measurement error increases rapidly. As in Ref. 14, we define the SNR as the ratio of the mean signal power at the peak of the Doppler burst to the noise power due to wall scatter and background

$$SNR = \frac{(AV)^2}{4N_0 \, \Delta f} = \frac{s_0^2 + q_0^2}{4n_0 \, (\Delta f / f_D)} \qquad (18)$$

where Δf is the noise bandwidth. (The noise bandwidth is determined by the low-pass and high-pass filters in the processor.)

Comparing this expression (eq. (18)) for the SNR with Eq. (17) allows us to express the SNR in terms of the relative error (σ_{f_D}/f_D) given by Eq. (9).

$$SNR = \frac{16}{\pi^{5/2} \, N^3} \left(\frac{f_D}{\Delta f}\right) \left(\frac{\sigma_{f_D}}{f_D}\right)^{-2} \qquad (19)$$

Even with SNR > 10, the counter will not provide measurements as accurate as indicated possible by the Cramer-Rao bound because of other error sources such as the finite clock frequency and the effectiveness of validation circuitry.

Numerical Examples

Two examples of calculating the Cramer-Rao bound and selecting the optimum aperture mask are presented in this section. The following parameters are used for both examples: the fluid velocity is 500 m/sec; the seed particles are polystyrene spheres with 1 μm diameter and real refractive index equal 1.59; no Bragg shift is used; the flow is perpendicular to the fringes; the laser power equals 0.1 W at 0.5145 μm wavelength; the beams are linearly polarized with the electric vector normal to the plane formed by the beams (along the y axis); and system efficiency including losses and PMT quantum efficiency is 10 percent. The wall is normal to the optical axis, is located 1 mm from the center of the probe volume, and is a Lambertian reflector with reflectivity equal $1/\pi$.

For the first example, which represents a low performance optical configuration: the focusing lens has a 200 mm focal length and a 50 mm diameter (f/4); the pinhole image diameter is set equal to 125 μm; the number of fringes is 12.5; the fringe spacing is 10 μm; and the uniform background radiance is 3.1×10^{-5} W/mm^2/sr.

For the second example, which represents a high performance optical configuration: the focusing lens has a 250 mm focal length and a 100 mm diameter (f/2.5); the pinhole image diameter is set equal to 70 μm; the number of fringes is 10; the fringe spacing is 5 μm; and the uniform background radiance is 3.8×10^{-3} W/mm^2/sr. Note that the background radiance is set higher for this example than it was for the first example. This was done to insure that the assumption that the noise is larger than the signal remains valid. Of course, this indicates a more severe environment.

For these numerical calculations, the the aperture plane is divided in 400 equal areas.

But, because of symmetry, only one quadrant need be considered with 100 area elements.

The error bound can be expressed in terms of these 100 elements as

$$\left(\frac{\sigma_{f_D}}{f_D}\right) = \frac{8}{\pi^{5/4} \, N^{3/2}} \left[\frac{\Sigma n_k}{\left(\Sigma s_k\right)^2 + \left(\Sigma q_k\right)^2}\right]^{1/2} \qquad (20)$$

where

$$n_k = n(x_k, y_k) \, \Delta A, \quad s_k = (x_k, y_k) \, \Delta A, \quad n_k = n(x_k, y_k) \, \Delta A \qquad (21)$$

The noise elements n_k and signal elements, s_k and q_k, are evaluated by numerically integrating Eqs. (12). Standard Mie scattering algorithms are used for the differential cross sections.

To determine the optimum aperture mask a numerical procedure is used to eliminate the set of areas that will maximize the quantity

$$Q = \frac{\left(\Sigma s_k\right)^2 + \left(\Sigma q_k\right)^2}{\Sigma n_k} \qquad (22)$$

The procedure used is to calculate Q using all the area elements, then eliminate each of the areas, one at a time, and recalculate Q. The area element whose elimination gives the greatest increase in Q is included in the aperture mask. This procedure is repeated until no further reduction in the error is possible. The resulting mask is the optimum for the particular distance from the probe volume to the wall.

The calculated masks for the two examples are shown in Fig. 6. The error bound (σ_{f_D}/f_D) = 0.05 and 0.002 for the f/4 and f/2.5 examples, respectively. (The noise bandwidth Δf was set equal to the Doppler frequency f_D.) The corresponding SNR = -7.1 dB and 25.8 dB, which means that a counter processor should be a suitable processor for the f/2.5 example, but not for the f/4 example. The mask covers 57 percent of the lens aperture for the f/4 optics and 51 percent for the f/2.5 optics. Also shown on Fig. 6 is the order that the grid elements are blocked in the optimization procedure.

Figure 7 illustrates how the SNR improves as the masks are built up. Note that the SNR improves less quickly as the masks approach their optimum configurations. This is particularly noticeable for the f/2.5 optics where the SNR would only be slightly decreased by using a mask that covers 20 percent of the lens aperture instead of the optimum mask which covers 51 percent.

Figure 8 shows the SNR as a function of distance from the probe volume to the wall (the SNR was calculated for the optimum mask at each location). Note that the SNR reaches a constant value at large distances because of the inclusion of a constant background radiance. This figure illustrates the improvement of the f/2.5 optics compared to the f/4 optics. With f/4 optics, measurements can be made to about 2 mm from the wall; while, with f/2.5 optics, measurements can be made to

about 0.5 mm. Of course, these results are dependent on the parameters chosen for the examples. In particular, the reflectivity of the wall has a large effect on the SNR for measurements near the wall.

Discussion

The optical design of a fringe-type laser anemometer for a particular experiment requires several steps to take into account all contraints imposed by the experiment and by the LA system. The initial step is to select a seed material that will follow the flow accelerations and will survive the flow environment. It is usually desirable to use monodisperse particles; however, this may be difficult to achieve in practice.

The next step is to select the fringe spacing and number of fringes. The fringe spacing must be such that the maximum velocity will not result in Doppler frequencies greater than the maximum frequency response of the photodetector and the signal processor. Furthermore, the minimum fringe spacing may be limited by the available solid viewing angle. (The fringe spacing is inversely proportional to the beam crossing angle and hence to the beam separation at the focusing lens.)

Another factor that can affect the selection of the fringe spacing is the phase cancellation that occurs when the scattered light is integrated over a large aperture. This can be a significant problem when the fringe spacing is on the order of the particle size. In fact, this phase cancellation is the basis for particle size measurements based on the visibility of the Doppler burst.[15,16]

The selection of the number of fringes is based on several considerations. For counter processors with a given time interval measurement accuracy (typically, 1 ns.), the number of cycles used must be large enough to result in an acceptable error on a single particle measurement. Note that the acceptable single particle measurement error will be larger for highly turbulent flows.[17]

The problem of statistical biasing, which occurs in turbulent flow, may also influence the selection of the number of fringes. For example, the biasing caused by flow angle fluctuations[18] is reduced by using a larger number of fringes. Also, the use of frequency shifting can reduce some biasing errors (but at the expense of increasing the required frequency response of the photo detector and signal processor).

After the number and spacing of the fringes have been established, the field stop (pinhole) can be sized to match the probe volume diameter. The focusing lens is selected based on the required working distance and available solid angle. It is generally advantageous to select as fast a lens as is practical.

With the optical system specified, the procedure presented in this paper for determining the optimum aperture mask can be applied. The mask should be optimized for the closest anticipated measurement position to the wall. Based on the calculated SNR, the suitability of a counter processor can be verified.

Note that to apply this procedure the bidirectional reflectivity of the surfaces in the test region must be known. Of course, the surfaces should be treated to minimize the reflectivity. (This can be accomplished either by absorbing the light or by reflecting the light in a "safe" direction.) For measurements near the window, the reflectivity of the window must also be known. These reflectivities will generally have to be obtained experimentally. It should be realized that the reflectivities can change during a test run as contaminants accumulate on the walls and windows. In addition, the background radiance due to flames, blackbody radiation, and multiple reflections of the laser light must be estimated or measured.

Finally, it should be noted that the assumption of spherical seed particles that was used for the Mie scattering calculations may introduce some error if the particles are not, in fact, spheres. And, if polydisperse particle size distributions are used, the analysis should be modified to take this into account.

Concluding Remarks

Using the analysis presented in this paper, the fringe-type laser anemometer can be evaluated in terms of its best possible performance based on the Cramer-Rao bound for the estimate of the variance of the measured Doppler frequency. The relation between this lower bound and the performance of counter-type processors points out the potential performance gain that should be achievable using more optimal processors for low signal-to-noise ratios.

APPENDIX A – CALCULATION OF NOISE

The irradiance at a point (x,y) on the aperture plane due to wall scatter is obtained by integrating the radiance L of the surface over the solid angle subtended by the image of the pinhole at the point on the aperture (fig. 3). For purposes of calculation, the aperture plane is assumed to be at the plane of the focusing lens instead of the position shown in Fig. 1. The light flux through area dA at point (x,y) on the aperture expressed in photoelectron counts per Doppler cycle is

$$n(x,y)dA =$$

$$\left(\frac{n\lambda}{hcf_D}\right) \int_{\Omega'} \left[L_r(x,y; \theta_r,\phi_r) + L_b\right] d\Omega \cos\theta \, dA \qquad (A1)$$

The radiance due to single scattering of the incident beams from the wall is

$$L_r(x,y;\theta_r,\phi_r) = \rho'(x',y';\theta_i,\phi_i;\theta_r,\phi_r) \, I_i(x',y')$$

$$(A2)$$

where $I(x',y')$ is the irradiance of the beams at the surface and ρ' is the bidirectional reflectivity. Note that ρ' is a function of both the direction of incident and the reflected light.

If the wall is normal to the optical axis, the irradiance of the Gaussian beams at the surface is

$$I_i(x',y') = \frac{P_\ell}{\pi}\left\{\frac{1}{w^2(z_1)}e^{-\frac{2(x_1^2+y_1^2)}{w^2(z_1)}}\right.$$

$$\left. + \frac{1}{w^2(z_2)}e^{-\frac{2(x_2^2+y_2^2)}{w^2(z_2)}}\right\} \qquad (A3)$$

where (x', y') is the point on the wall along the ray through point (x,y) in the direction (θ,ϕ). Also, (x_1, y_1, z_1) and (x_2, y_2, z_2) are the coordinates of the point on the wall in coordinate system with z_1 and z_2 along the beam propagation directions and are given by

$$\begin{bmatrix} x_{1,2} \\ y_{1,2} \\ z_{1,2} \end{bmatrix} = \begin{bmatrix} \cos\beta & 0 & \pm\sin\beta \\ 0 & 1 & 0 \\ \mp\sin\beta & 0 & \cos\beta \end{bmatrix} \begin{bmatrix} x' \\ y' \\ d \end{bmatrix} \qquad (A4)$$

with d being the distance from the focal point to the wall and $w(z)$ the beam radius given by

$$w(z) = w_0\left[1 + \left(\frac{\lambda z}{\pi w_0^2}\right)^2\right]^{1/2} \qquad (A5)$$

APPENDIX B – CALCULATION OF SIGNAL

The signal is calculated using Mie scattering theory,[19] which takes into account both the variation in the amplitude and phase of the scattered fields as a function of scattering angle. The incident beams are located in the x-z plane and have a crossing angle 2β (fig. 4).

The electric fields of the incident beams near the waists are represented as plane waves

$$\underline{E}_{1,2} = \hat{e}_{1,2} E_{01,02}\, e^{i2\pi f_{1,2}t - i\underline{k}_{1,2}\cdot\underline{r}} \qquad (B1)$$

where the field amplitudes are $E_{01,02} = (2Z_0)^{1/2} I_0$; with I_0 being the peak irradiance of each beam at its waist, which is related to the laser power and waist diameter by $I_0 = P_\ell/\pi w_0^2$. The electric fields of the beams are assumed to be plane polarized with unit vectors $\hat{e}_1$ and $\hat{e}_2$.

We define the following unit vectors:

$$\hat{s}_{1,2} = (\underline{k}_s \times \underline{k}_{1,2})\Big/\left|\underline{k}_s \times \underline{k}_{1,2}\right| \qquad (B2)$$

$$\hat{p}_{1,2} = (\underline{k}_{1,2} \times \hat{s}_{1,2})/k \qquad (B3)$$

$$\hat{q}_{1,2} = (\underline{k}_s \times \hat{s}_{1,2})/k \qquad (B4)$$

where $\hat{s}_1$ and $\hat{s}_2$ are normal to the scattering planes; $\hat{p}_1$ and $\hat{p}_2$ are normal to the propagation directions of the incident beams and in the scattering planes; and, $\hat{q}_1$ and $\hat{q}_2$ are normal to the scattered wave propagation direction and in the scattering planes.

The incident fields can be expressed in terms of the components in the scattering plane and normal to the scattering plane

$$\underline{E}_{1,2} = E_{1s,2s}\,\hat{s}_{1,2} + E_{1p,2p}\,\hat{p}_{1,2} \qquad (B5)$$

The scattered fields are given by Mie scattering theory for spheres[19]

$$\underline{E}_{1,2}^{(s)} = \frac{i\,e^{-ikR}}{kR}\left[E_{1s,2s}\,S_s(\theta_{1,2})\,\hat{s}_{1,2}\right.$$

$$\left. + E_{1p,2p}\,S_p(\theta_{1,2})\,\hat{q}_{1,2}\right] \qquad (B6)$$

where R is the distance from the scatterer to the observation point, and $S_s(\theta)$ and $S_p(\theta)$ are the usual Mie scattering amplitude functions with the scattering angles given by

$$\cos\theta_{1,2} = (\underline{k}_{1,2} \cdot \underline{k}_s)/k^2 \qquad (B7)$$

The irradiance of the scattered light at the observation point is

$$I_s(x,y) = \left|E_1^{(s)} + E_2^{(s)}\right|^2/2Z_0 = I_{sdc} + I_{sac} \qquad (B8)$$

This is composed of the sum of a slowly varying dc component, I_{sdc}, corresponding to the pedestal of the Doppler burst and an ac component, I_{sac}, modulated at the Doppler frequency. These can be written as

$$I_{sdc}(x,y) = I_0\left[(\hat{e}_1\cdot\hat{s}_1)^2\,\sigma_s(\theta_1) + (\hat{e}_1\cdot\hat{p}_1)^2\,\sigma_p(\theta_1)\right.$$

$$\left. + (\hat{e}_2\cdot\hat{s}_2)^2\,\sigma_s(\theta_2) + (\hat{e}_2\cdot\hat{p}_2)^2\,\sigma_p(\theta_2)\right] \qquad (B9)$$

$$I_{sac}(x,y) = I_0\sum_{\substack{\alpha=s,p \\ \beta=s,p}}\sigma_{\alpha\beta}$$

$$(\cos\delta_{\alpha\beta}\cos 2\pi f_D t - \sin\delta_{\alpha\beta}\sin 2\pi f_D t) \qquad (B10)$$

Note that I_{sac} is expressed in a quadrature representation form. Because the phase of I_{sac} varies across the aperture, the detected signal will, in general, be less than the signal that would be detected if the phase were constant.

The Mie complex amplitude functions can be written as

$$S_\alpha(\theta) = \left|S_\alpha(\theta)\right|e^{i\delta_\alpha(\theta)}, \quad \alpha = s,p \qquad (B11)$$

The differential cross sections for "s" and "p" scattering are

$$\sigma_\alpha(\theta) = (\lambda/2\pi)\,|S_\alpha(\theta)|^2, \quad \alpha = s,p \qquad (B12)$$

In Eq. (B10) we also introduced the following

$$\sigma_{ss} = [\sigma_s(\theta_1)\,\sigma_s(\theta_2)]^{1/2}\,(\hat{e}_1\cdot\hat{s}_1)\,(\hat{e}_2\cdot\hat{s}_2)\,(\hat{s}_1\cdot\hat{s}_2)$$

7

$$\sigma_{pp} = [\sigma_p(\theta_1)\ \sigma_p(\theta_2)]^{1/2}\ (\hat{e}_1 \cdot \hat{p}_1)\ (\hat{e}_2 \cdot \hat{p}_2)\ (\hat{q}_1 \cdot \hat{q}_2)$$

$$\sigma_{sp} = [\sigma_s(\theta_1)\ \sigma_p(\theta_2)]^{1/2}\ (\hat{e}_1 \cdot \hat{s}_1)\ (\hat{e}_2 \cdot \hat{p}_2)\ (\hat{s}_1 \cdot \hat{q}_2)$$

$$\sigma_{ps} = [\sigma_p(\theta_1)\ \sigma_s(\theta_2)]^{1/2}\ (\hat{e}_1 \cdot \hat{p}_1)\ (\hat{e}_2 \cdot \hat{s}_2)\ (\hat{q}_1 \cdot \hat{s}_2)$$

$$\delta_{\alpha\beta} = \delta_\alpha(\theta_1) - \delta_\beta(\theta_2), \qquad \alpha,\beta = s,p \qquad (B13)$$

References

1. Schodl, R., "Laser Dual-Beam Method for Flow Measurements in Turbomachines," ASME Paper 74-GT-157, Mar. 1974.
2. Lading, L., "Estimating Time and Time-Lag in Time-of-Flight Velocimetry," Applied Optics, Vol. 22, No. 22, Nov. 15, 1983, pp. 3637-3643.
3. Goldman, L. J., and Seasholtz, R. G., "Comparison of Laser Anemometer Measurements and Theory in an Annular Turbine Cascade with Experimental Accuracy Determined by Parameter Estimation," Engineering Applications of Laser Velocimetry, edited by H. W. Coleman and P. A. Pfund, ASME, 1982, pp. 83-92.
4. Goldman, L. J., and Seasholtz, R. G., "Laser Anemometer Measurements in an Annular Cascade of Core Turbine Vanes and Comparison with Theory," NASA TP-2018, 1982.
5. Powell, J. A., Strazisar, A. J., and Seasholtz, R. G., "High-Speed Laser Anemometer System for Intrarotor Flow Mapping in Turbomachinery," NASA TP-1663, 1982.
6. Powell, J. A., Strazisar, A. J., and Seasholtz, R. G., "Efficient Laser Anemometer for Intra-Rotor Flow Mapping in Turbomachinery," Journal of Engineering for Power, Vol. 103, No. 2, Apr. 1981, pp. 424-429.
7. Gardavsky, J., and Kleine, R., "Reflection Suppression by Polarization in Backscatter LDA Measurements Near Walls and in Two-Phase Flows," Applied Optics, Vol. 20., No. 23, Dec. 1, 1981, pp. 4110-4123.
8. Gardavsky, J., and Bok, J., "Scattering of Circularly Polarized Light in Laser Doppler Anemometry," Applied Optics, Vol. 21, No. 1, Jan. 1, 1982, pp. 158-165.
9. Mishina, H., Vlachos, N. S., and Whitelaw, J. H., "Effect of Wall Scattering on SNR in Laser Doppler Anemometry," Applied Optics, Vol. 18, July 15, 1979, pp. 2480-2485.
10. Mishina, H., Takahashi, K., and Asakura, T., "Effect of Wall Scattering on SNR in Off-Axis Differential-Type Laser Doppler Velocimetry," Optical and Quantum Electronics, Vol. 15, Sept. 1983, pp. 419-431.
11. Eckbreth, A. C., and Davis, J. W., "Spatial Resolution Enhancement in Coaxial Light Scattering Geometries - Raman Laser Diagnostics," Applied Optics, Vol. 16, Apr. 1977, pp. 804-806.
12. Whalen, A. D., Detection of Signals in Noise, Academic Press, New York, 1971, pp. 324-331.
13. Lading, L., and Jensen, A. S., "Estimating the Spectral Width of a Narrowband Optical Signal," Applied Optics, Vol. 19, Aug. 15, 1980, pp. 2750-2756.
14. Adrian, R. J., Humphrey, J. A. C., and Whitelaw, J. H., "Frequency Measurement Errors Due to Noise in LDV Signals," in The Accuracy of Flow Measurements by Laser Doppler Methods, edited by P. Buchhave, J. M. Delhaye, F. Durst, W. K. George, K. Refslund, and J. H. Whitelaw, Proceedings in LDA-Symposium Copenhagen, Skovlunde, Denmark, 1976, pp. 287-311.
15. Chu, W. P., and Robinson, D. M., "Scattering from a Moving Spherical Particle by Two Crossed Coherent Plane Waves," Applied Optics, Vol. 16, Mar. 1977, pp. 619-626.
16. Adrian, R. J., and Orloff, K. L., "Laser Anemometer Signals: Visibility Characteristics and Application to Particle Sizing," Applied Optics, Vol. 16, Mar. 1977, pp. 677-684.
17. Edwards, R. V., and Jensen, A. S., "Particle-Sampling Statistics in Laser Anemometers Sample-and-Hold Systems and Saturable Systems," Journal of Fluid Mechanics, Vol. 133, Aug. 1983, pp. 397-411.
18. Seasholtz, R. G., "Laser Doppler, Velocimeter System for Turbine Stator Cascade Studies and Analysis of Statistical Biasing Errors," NASA TN D-8297, 1977.
19. Van de Hulst, H. C., Light Scattering by Small Particles, Dover Publications, New York, 1981, Chapter 9.
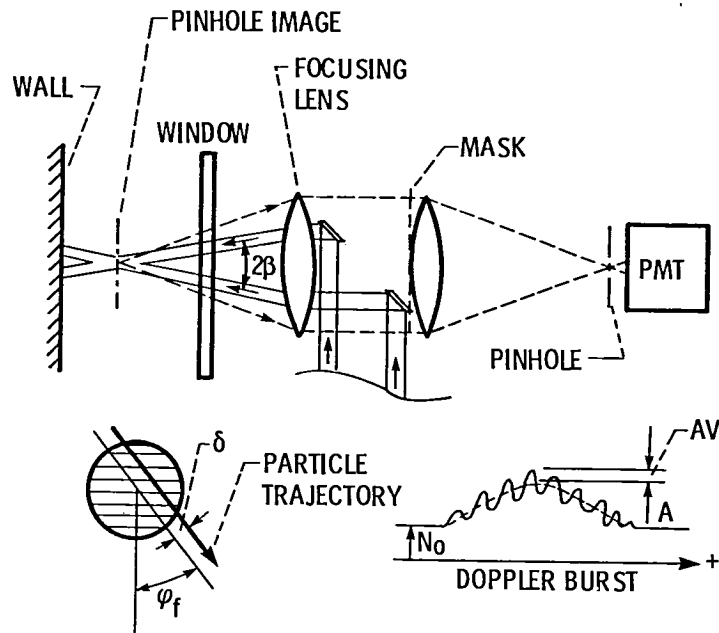
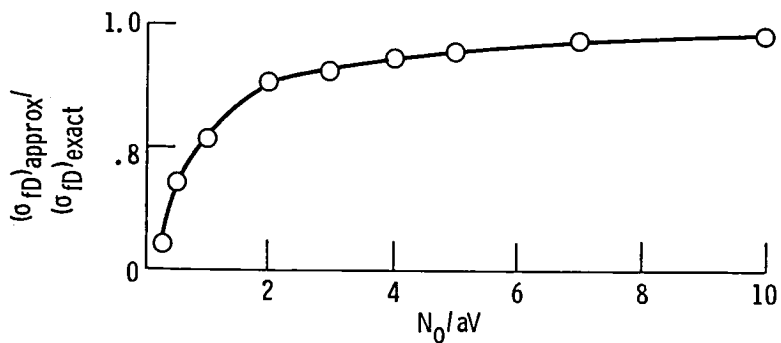Figure 1. - Optical configuration of coaxial backscatter fringe-type laser anemometer.

Figure 2. - Ratio of approximate value (eq. 9) to exact value (eq. 3) of lower bound for relative error of Doppler frequency versus ratio of background amplitude to signal amplitude. Parameters used in calculation are: number fringes, $N = 10$; signal amplitude, $aV = 50$ counts/Doppler cycle; visibility, $V = 1$; and, phase, $\phi = 0$.
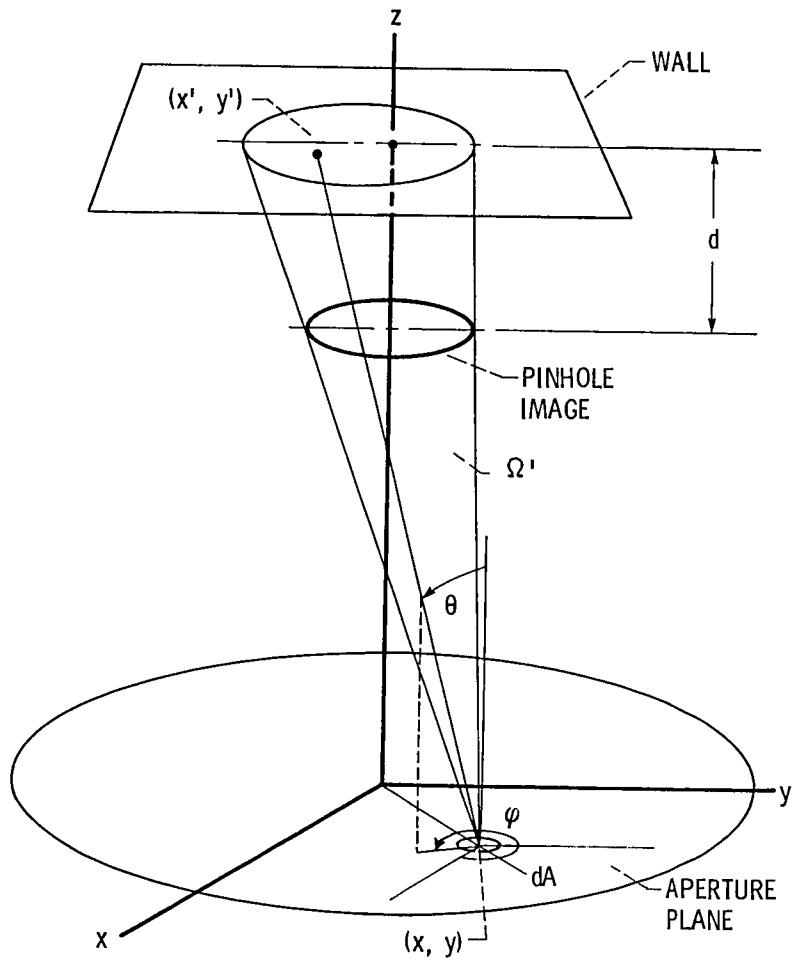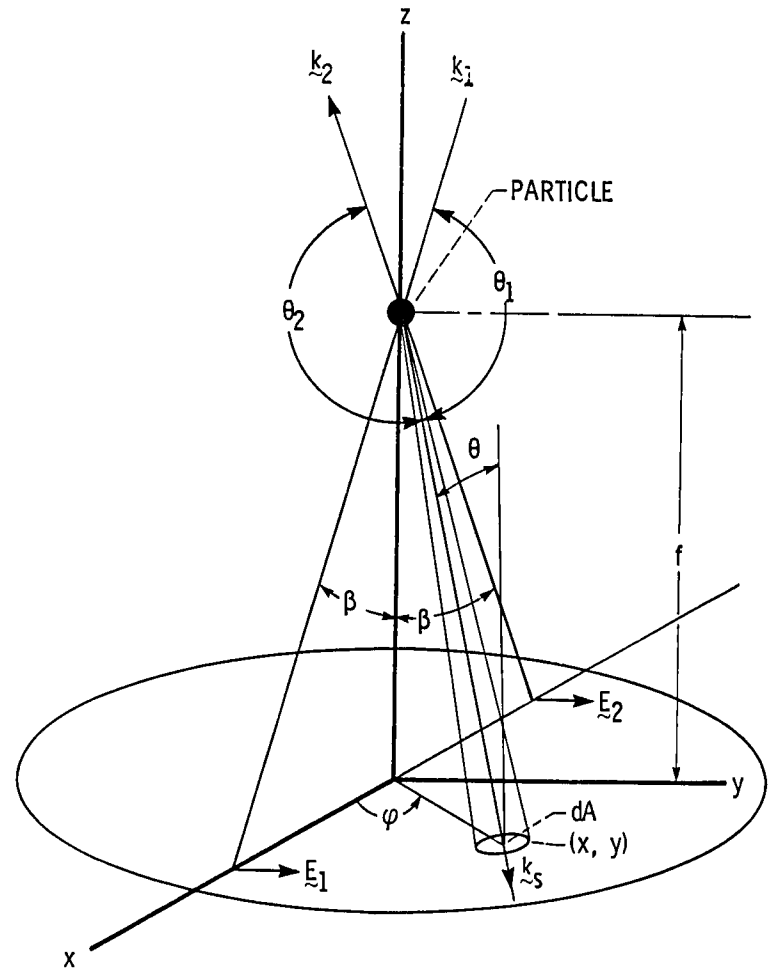
Figure 3. - Geometry used for evaluation of wall scatter noise.

Figure 4. - Geometry used for evaluation of Mie scattering.

(a) Diameter d = 0.5 μm; σ (180°) = 0.1873x10^{-13} m^2.

(b) Diameter d = 1.0 μm; σ(180°) = 0.3695x10^{-12} m^2.

(c) Diameter d = 1.5 μm; σ(180°) = 0.2169x10^{-11} m^2.
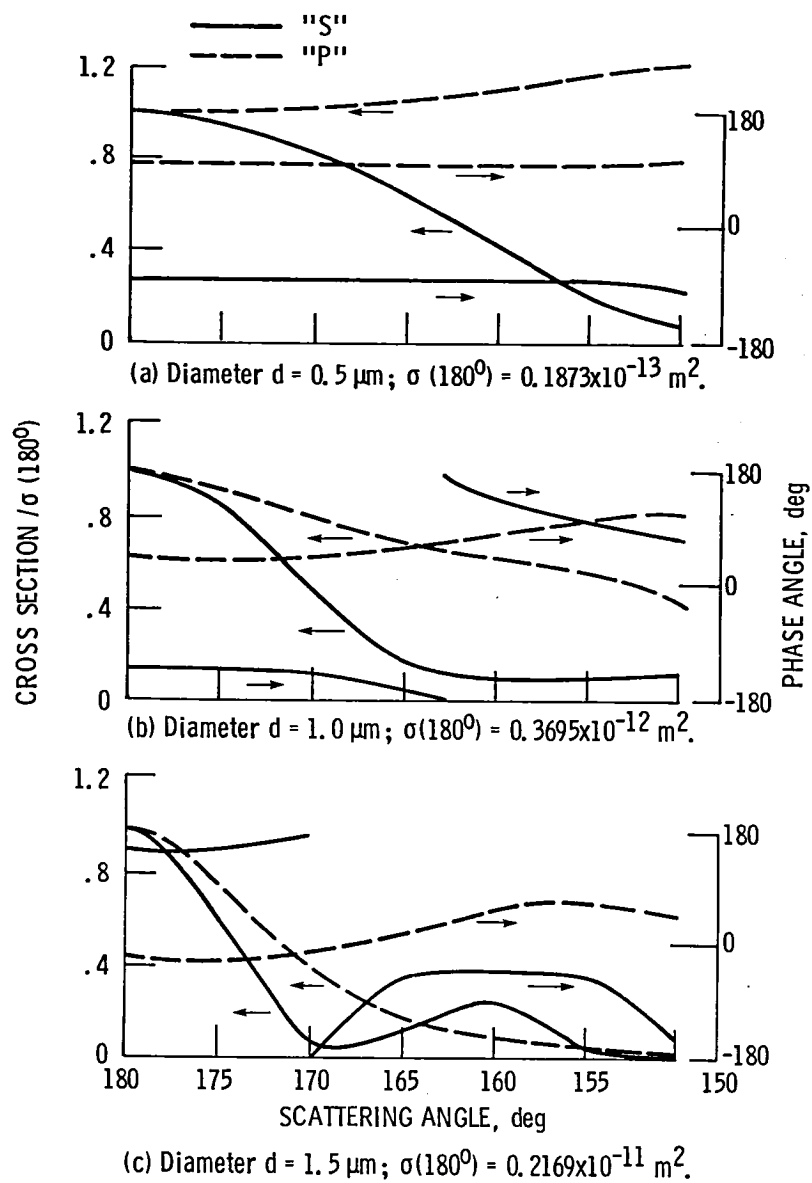
Figure 5. – Differential scattering cross section and
phase versus scattering angle for polystyrene spheres
(n = 1.59). Wavelength λ = 0.5145 μm.
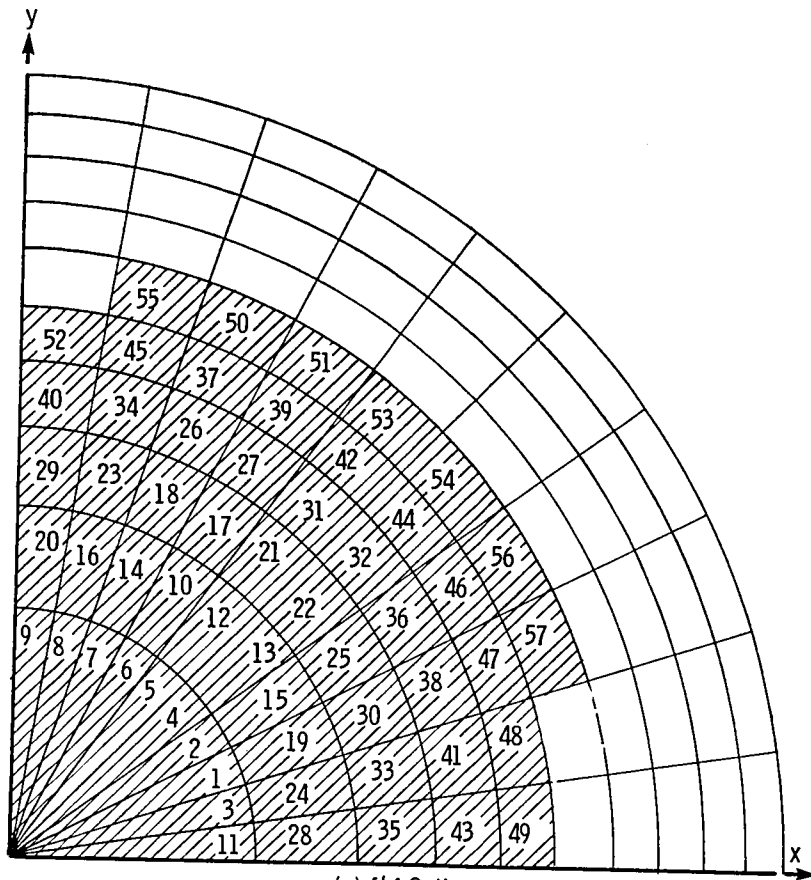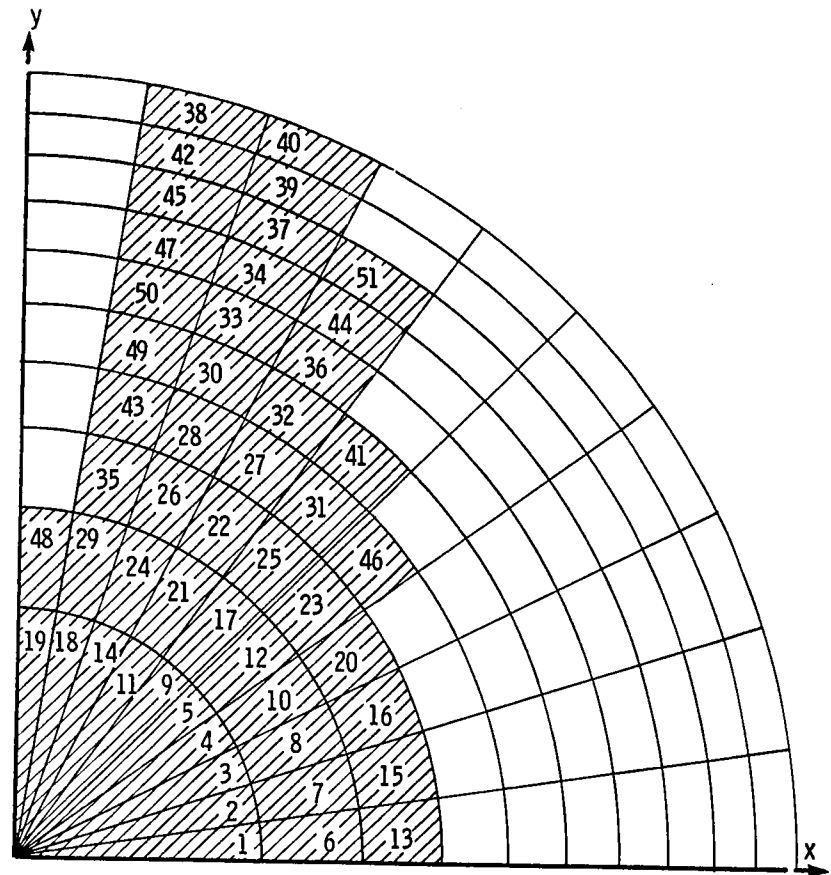
(a) f/4 Optics.

Figure 6. – Optimum masks for probe volume located 1 mm from wall. Grid elements are numbered in the order that the mask is built up.

(b) f/2.5 Optics.

Figure 6. – Concluded.
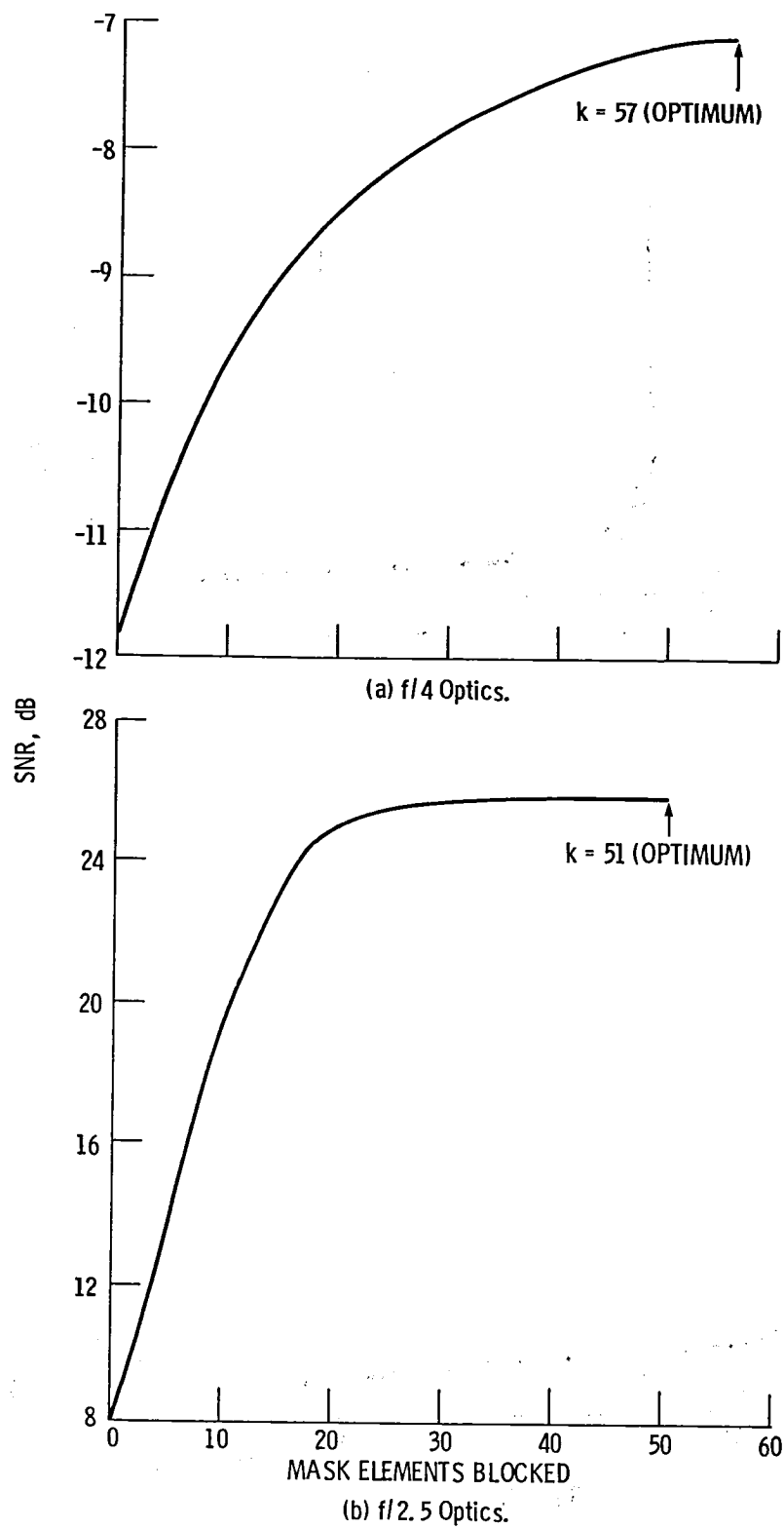
Figure 7. – Signal-to-noise ratio (SNR) versus accumulation of mask area elements.
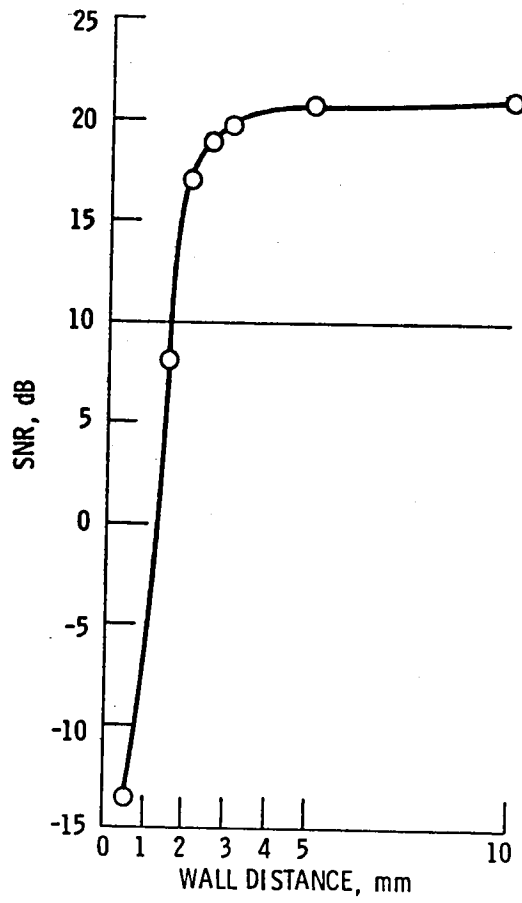
(a) f/4 Optics.

Figure 8. – Signal-to-noise ratio (SNR)
for optimum mask versus distance of
probe volume from wall.
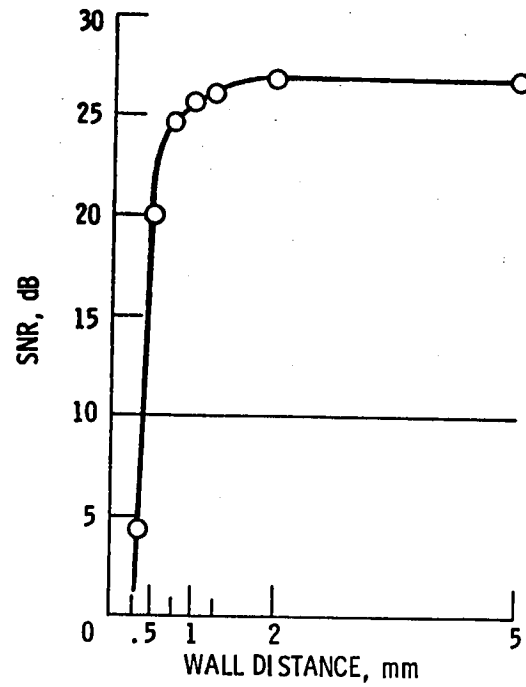
(b) f/2. 5 Optics.

Figure 8. – Concluded

1. Report No. NASA TM-83658 AIAA-84-1459	2. Government Accession No.	3. Recipient's Catalog No.
4. Title and Subtitle Optimization of Fringe-Type Laser Anemometers for Turbine Engine Component Testing		5. Report Date
		6. Performing Organization Code 533-04-1A
7. Author(s) Richard G. Seasholtz, Lawrence G. Oberle, and Donald H. Weikle		8. Performing Organization Report No. E-2099
		10. Work Unit No.
9. Performing Organization Name and Address National Aeronautics and Space Administration Lewis Research Center Cleveland, Ohio 44135		11. Contract or Grant No.
		13. Type of Report and Period Covered Technical Memorandum
12. Sponsoring Agency Name and Address National Aeronautics and Space Administration Washington, D.C. 20546		14. Sponsoring Agency Code

15. Supplementary Notes

16. Abstract

The fringe-type laser anemometer is analyzed using the Cramer-Rao bound for the variance of the estimate of the Doppler frequency as a figure-of-merit. Mie scattering theory is used to calculate the Doppler signal wherein both the amplitude and phase of the scattered light are taken into account. The noise from wall scatter is calculated using the wall bidirectional reflectivity and the irradiance of the incident beams. A procedure is described to determine the optimum aperture mask for the probe volume located a given distance from a wall. The expected performance of counter-type processors is also discussed in relation to the Cramer-Rao bound. Numerical examples are presented for a coaxial backscatter anemometer.

17. Key Words (Suggested by Author(s)) Laser anemometers Laser velocimeters	18. Distribution Statement Unclassified - unlimited STAR Category 35

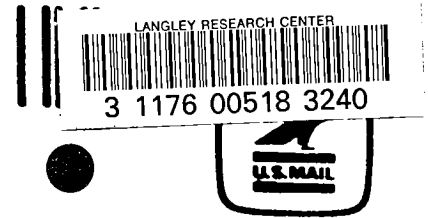| 19. Security Classif. (of this report) Unclassified	20. Security Classif. (of this page) Unclassified	21. No. of pages	22. Price*
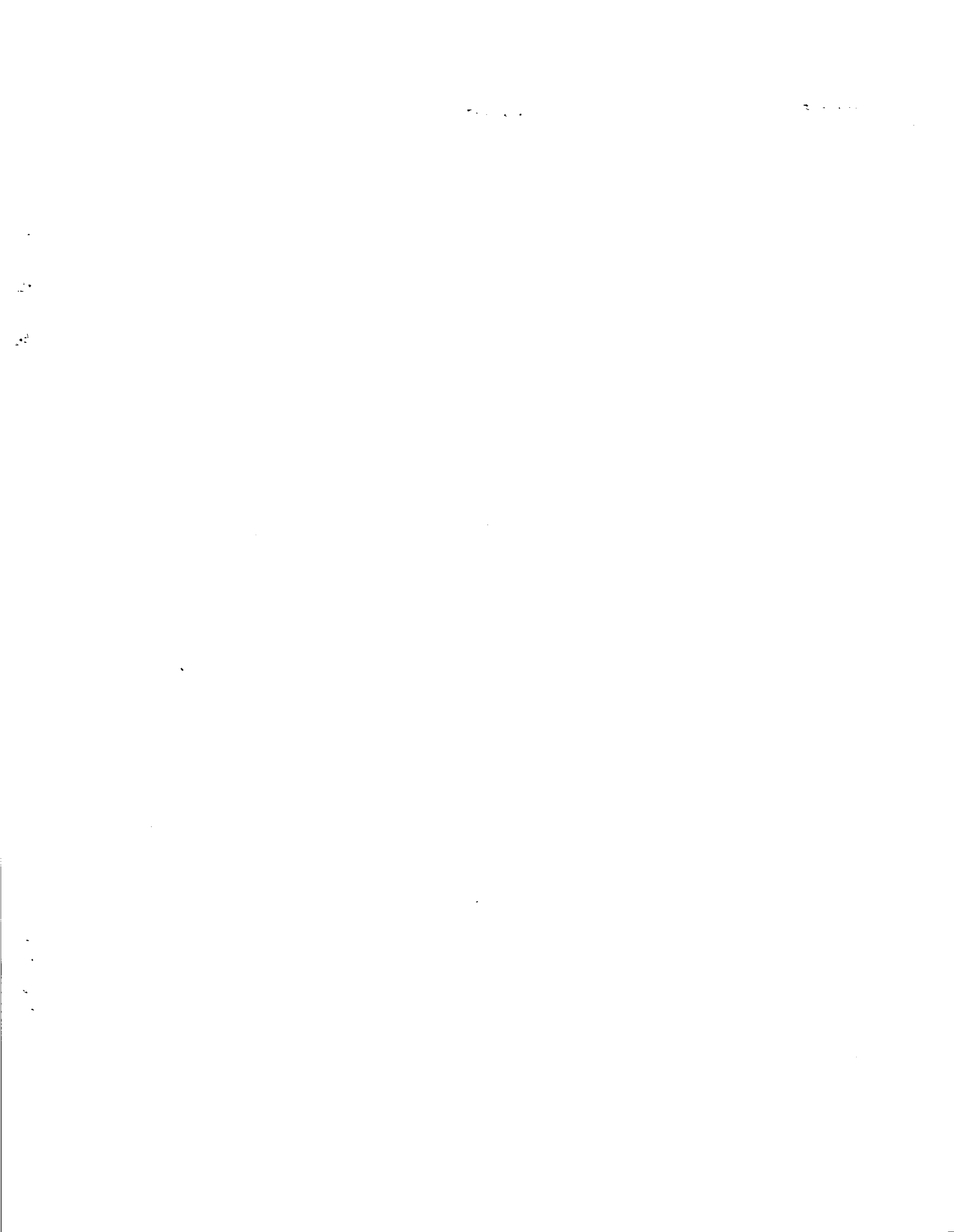
National Aeronautics and
Space Administration

Washington, D.C.
20546

SPECIAL FOURTH CLASS MAIL
BOOK

NASA

POSTMASTER: If Undeliverable (Section 158
Postal Manual) Do Not Return